The Astrophysical Journal Supplement Series, 276:1 (14pp), 2025 January https://doi.org/10.3847/1538-4365/ad8e3d

Multiband Optical Variability of the Blazar 3C 454.3 on Diverse Timescales

Karan Dogra[1,2], Alok C. Gupta[1,3], C. M. Raiteri[4], M. Villata[4], Paul J. Wiita[5], S. O. Kurtanidze[6], S. G. Jorstad[7,8], R. Bachev[9], G. Damljanovic[10], C. Lorey[11], S. S. Savchenko[8,12,13], O. Vince[10], M. Abdelkareem[14], F. J. Aceituno[15], J. A. Acosta-Pulido[16,17], I. Agudo[15], G. Andreuzzi[18], S. A. Ata[14], G. V. Baida[19], L. Barbieri[20], D. A. Blinov[21,22], G. Bonnoli[15,23], G. A. Borman[24], M. I. Carnerero[4], D. Carosati[18,25], V. Casanova[15], W. P. Chen[26], Lang Cui[3], E. G. Elhosseiny[14], D. Elsaesser[11,27], J. Escudero[15], M. Feige[11], K. Gazeas[28], L. E. Gennadievna[8], T. S. Grishina[8], Minfeng Gu[29], V. A. Hagen-Thorn[8], F. Hemrich[11], H. Y. Hsiao[26], M. Ismail[14], R. Z. Ivanidze[6], M. D. Jovanovic[10], T. M. Kamel[14], G. N. Kimeridze[6], E. N. Kopatskaya[8], D. Kuberek[11], O. M. Kurtanidze[6,30], A. Kurtenkov[9], V. M. Larionov[8], L. V. Larionova[8], M. Liao[31,32,33], H. C. Lin[26], K. Mannheim[11,34], A. Marchini[35], C. Marinelli[36], A. P. Marscher[7], D. Morcuende[15], D. A. Morozova[8], S. V. Nazarov[24], M. G. Nikolashvili[6], D. Reinhart[11], J. O. Santos[15], A. Scherbantin[11,34], E. Semkov[9], E. V. Shishkina[8], L. A. Sigua[6], A. K. Singh[2], A. Sota[15], R. Steineke[11], M. Stojanovic[10], A. Strigachev[9], A. Takey[14], Amira A. Tawfeek[14], I. S. Troitskiy[8], Y. V. Troitskaya[8], An-Li Tsai[26,37], A. A. Vasilyev[8], K. Vrontaki[28], Zhongli Zhang[29,38], A. V. Zhovtan[19], N. Zottmann[11], and Wenwen Zuo[29]

[1] Aryabhatta Research Institute of Observational Sciences (ARIES), Manora Peak, Nainital 263001, India; karandogra987@gmail.com, acgupta30@gmail.com
[2] Department of Applied Physics, Mahatma Jyotiba Phule Rohilkhand University, Bareilly 243006, India
[3] Xinjiang Astronomical Observatory, Chinese Academy of Sciences, 150 Science-1 Street, Urumqi 830011, People's Republic of China
[4] INAF, Osservatorio Astrofisico di Torino, via Osservatorio 20, I-10025 Pino Torinese, Italy
[5] Department of Physics, The College of New Jersey, P.O. Box 7718, Ewing, NJ 08628, USA
[6] Abastumani Observatory, Mt. Kanobili, 0301 Abastumani, Georgia
[7] Institute for Astrophysical Research, Boston University, 725 Commonwealth Avenue, Boston, MA 02215, USA
[8] Astronomical Institute, Saint Petersburg State University, 7/9 Universitetskaya nab., St. Petersburg, 199034, Russia
[9] Institute of Astronomy and National Astronomical Observatory, Bulgarian Academy of Sciences, 72 Tsarigradsko shosse Blvd., 1784 Sofia, Bulgaria
[10] Astronomical Observatory, Volgina 7, 11060 Belgrade, Serbia
[11] Hans-Haffner-Sternwarte, Naturwissenschaftliches Labor für Schüler am FKG, Friedrich-Koenig-Gymnasium, D-97082 Würzburg, Germany
[12] Special Astrophysical Observatory, Russian Academy of Sciences, 369167, Nizhnii Arkhyz, Russia
[13] Pulkovo Observatory, St. Petersburg, 196140, Russia
[14] National Research Institute of Astronomy and Geophysics (NRIAG), 11421 Helwan, Cairo, Egypt
[15] Instituto de Astrofísica de Andalucía, IAA-CSIC, Glorieta de la Astronomía s/n, E-18008 Granada, Spain
[16] Instituto de Astrofísica de Canarias (IAC), E-38200 La Laguna, Tenerife, Spain
[17] Universidad de La Laguna, Departamento de Astrofísica, E-38206 La Laguna, Tenerife, Spain
[18] INAF, TNG Fundación Galileo Galilei, La Palma, E-38712, Spain
[19] Crimean Astrophysical Observatory of the Russian Academy of Sciences, P/O Nauchny 298409, Crimea[†]
[20] Orciatico Astronomical Observatory, Orciatico (Pisa), Italy
[21] Institute of Astrophysics, Foundation for Research and Technology—Hellas, Voutes, 70013 Heraklion, Greece
[22] Department of Physics, University of Crete, 71003, Heraklion, Greece
[23] INAF Osservatorio Astronomico di Brera, Via E. Bianchi 46, 23807 Merate (LC), Italy
[24] Crimean Astrophysical Observatory of the Russian Academy of Sciences, P/O Nauchny 298409, Russia[†]
[25] EPT Observatories, Tijarafe, La Palma, E-38780, Spain
[26] Institute of Astronomy, National Central University, Taoyuan 32001, Taiwan
[27] Astroteilchenphysik, TU Dortmund, Otto-Hahn-Str. 4A, D-44227 Dortmund, Germany
[28] Section of Astrophysics, Astronomy and Mechanics, Department of Physics, National and Kapodistrian University of Athens, GR-15784 Zografos, Athens, Greece
[29] Shanghai Astronomical Observatory, Chinese Academy of Sciences, 80 Nandan Road, Shanghai 200030, People's Republic of China
[30] Engelhardt Astronomical Observatory, Kazan Federal University, Tatarstan, Russia
[31] National Astronomical Observatories, Chinese Academy of Sciences, 20A Datun Road, Chaoyang District, Beijing 100101, People's Republic of China
[32] Chinese Academy of Sciences South America Center of Astronomy, National Astronomical Observatories, CAS, Beijing 100101, People's Republic of China
[33] Instituto de Estudios Astrofisicos, Facultad de Ingenieria y Ciencias, Universidad Diego Portales, Av. Ejército 441, Santiago, Chile
[34] Lehrstuhl für Astronomie, Universität Würzburg, D-97074 Würzburg, Germany
[35] University of Siena, Astronomical Observatory, Via Roma 56. 53100, Siena, Italy
[36] Dip. di Scienze Fisiche, della Terra e dell'Ambiente, Universitá di Siena, Via Roma 56, 53100, Siena, Italy
[37] Department of Physics, National Sun Yat-sen University, Kaohsiung, 80424, Taiwan
[38] Key Laboratory of Radio Astronomy and Technology, Chinese Academy of Sciences, A20 Datun Road, Chaoyang District, Beijing 100101, People's Republic of China

Received 2024 August 28; revised 2024 October 15; accepted 2024 October 31; published 2024 December 9

[†] While the AAS journals adhere to and respect UN resolutions regarding the designations of territories (available at http://www.un.org/press/en), it is our policy to use the affiliations provided by our authors on published articles.

Abstract

Due to its peculiar and highly variable nature, the blazar 3C 454.3 has been extensively monitored by the WEBT team. Here, we present for the first time these long-term optical flux and color variability results using data acquired in *B*, *V*, *R*, and *I* bands over a time span of about two decades. We include data from WEBT collaborators and public archives such as SMARTS, Steward Observatory, and Zwicky Transient Facility. The data are binned and segmented to study the source over this long term when more regular sampling was available. During our study, the long-term spectral variability reveals a redder-when-brighter trend, which, however, stabilizes at a particular brightness cutoff of ∼14.5 mag in the *I* band, after which it saturates and evolves into a complex state. This trend indicates increasing dominance of jet emission over accretion disk (AD) emission until jet emission completely dominates. Plots of the variation in spectral index (following $F_\nu \propto \nu^{-\alpha}$) reveal a bimodal distribution using a one-day binning. These correlate with two extreme phases of 3C 454.3, an outburst or high-flux state and a quiescent or low-flux state, which are respectively jet- and AD-dominated. We have also conducted intraday variability studies of nine light curves and found that six of them are variable. Discrete correlation function analysis between different pairs of optical wave bands peaks at zero lags, indicating cospatial emission in different optical bands.

Unified Astronomy Thesaurus concepts: Active galactic nuclei (16); Blazars (164); Flat-spectrum radio quasars (2163); Markov chain Monte Carlo (1889); Relativistic jets (1390); Supermassive black holes (1663)

Materials only available in the online version of record: animation

1. Introduction

Blazars, a distinct subclass of radio-loud active galactic nuclei (AGNs), exhibit flux changes over the whole electromagnetic (EM) spectrum, covering time intervals from minutes to several years. This category of AGN is further divided into BL Lacertae (BL Lac) objects and flat-spectrum radio quasars (FSRQs). BL Lac objects have essentially nonexistent or very weak emission lines (equivalent widths $\leqslant$5 Å) in their ultraviolet (UV) to optical spectra (J. T. Stocke et al. 1991; M. J. M. Marcha et al. 1996), whereas FSRQs are characterized by significant emission lines (R. D. Blandford & M. J. Rees 1978; G. Ghisellini et al. 1997). The multiwavelength spectral energy distribution (SED) of blazars is double-hump shaped (e.g., C. von Montigny et al. 1995; G. Fossati et al. 1998). According to the location of the first hump peak, blazars have been more recently classified into three subclasses: low synchrotron frequency peaked (LSP) blazars, intermediate synchrotron frequency peaked (ISP) blazars, and high synchrotron frequency peaked (HSP) blazars. For LSP blazars, the synchrotron peak frequency (ν_{sy}) of the first hump peak is $\nu_{sy} \leqslant 10^{14}$ Hz; for ISP blazars, it is 10^{14} Hz $\leqslant \nu_{sy} \leqslant 10^{15}$ Hz; and HSP blazars have $\nu_{sy} \geqslant 10^{15}$ Hz (A. A. Abdo et al. 2010). The first hump of the SED is due to the synchrotron emission from the electrons in the relativistic jet. The second hump is widely accepted as coming from the inverse Compton scattering of either the photons emitted by the synchrotron process responsible for the first hump (synchrotron self-Compton) or photons emerging from the accretion disk (AD), emission lines, or dusty torus (external Compton) (e.g., M.-H. Ulrich et al. 1997; M. Böttcher 2007). Aside from these leptonic models, the second hump may be explained by hadronic models, which involve emission from relativistic protons or muon synchrotron radiation (A. Mücke et al. 2003).

Blazar jets are oriented nearly along the viewer's line of sight, resulting in the detected radiation being significantly Doppler-enhanced (e.g., C. M. Urry & P. Padovani 1995). The majority of blazar emissions across the EM spectrum are nonthermal. But in FSRQs, a bump is sometimes seen to rise above them from ∼1 μm and to cut off below 0.6 keV, which is called the big blue bump (BBB; G. A. Shields 1978; J. N. Bregman 1990). Two emission mechanisms have been seriously proposed for the BBB: optically thin thermal free–free radiation (e.g., R. Antonucci & R. Barvainis 1990; G. J. Ferland et al. 1990; R. Barvainis 1993; S. Collin-Souffrin et al. 1996) and optically thick thermal radiation from the AD (e.g., G. A. Shields 1978; M. A. Malkan & W. L. W. Sargent 1982; B. Czerny & M. Elvis 1987; A. Laor & H. Netzer 1989).

It has been shown over the past few decades that blazars exhibit variations in flux, spectrum, and polarization in all EM bands that are accessible on time spans from a couple of minutes to many years (e.g., A. Agarwal et al. 2015; A. C. Gupta et al. 2016, 2017; V. Dhiman et al. 2024). Blazar variability on timescales ranging from a few minutes to less than a day is referred to as microvariability (H. R. Miller et al. 1989) or intraday variability (IDV; S. J. Wagner & A. Witzel 1995). Blazar variability on timescales ranging from a few days to several weeks is referred to as short-term variability (STV), while variability over months to decades is referred to as long-term variability (LTV; A. C. Gupta et al. 2004). Most of the variability shown by blazars in the EM spectrum is characterized by nonlinearity, stochasticity, and a lack of periodicity (e.g., P. Kushwaha et al. 2017b).

Earlier studies reveal that, in general, there are two types of trends of spectral variation in blazars, with BL Lac objects often showing bluer-when-brighter (BWB) behavior (e.g., C. S. Stalin et al. 2006; M. Gu & Y. L. Ai 2011; H. Gaur et al. 2012a) and FSRQs frequently becoming redder when brighter (RWB) (e.g., M. F. Gu et al. 2006; E. Bonning et al. 2012) trends. Nonetheless, some studies have found opposite trends, i.e., FSRQs following BWB (M. Gu & Y. L. Ai 2011) and BL Lac objects following RWB. Some previous studies also suggested that the long-term color variability of BL Lac objects has no definite trend (M. Villata et al. 2002, 2004; C. S. Stalin et al. 2006; C. M. Raiteri et al. 2021, 2023), or achromatic behavior. A study conducted by B.-K. Zhang et al. (2015), using a sample of 49 FSRQs and 22 BL Lac objects from the SMARTS monitoring program, found that 35 FSRQs and 11 BL Lac objects respectively followed RWB and BWB trends. The majority of these studies lack a sufficient number of quasi-simultaneous data points or have been conducted over a short period of time. This motivated us to study the dichotomous color behavior of blazars along with their flux variability over diverse timescales. We wanted to investigate whether there is a long-term trend in color with flux that can be well studied with an extensive data set or whether a smooth transition is possible in color–magnitude (CM) space.

Table 1
Optical Data Sets from Different Observatories with Aperture Size and Filters Used

Observatory	MJD Start	MJD Stop	Origin	Aperture (cm)	Filters	Data Points (N_{obs})	Marker	Color
Abastumani	58501.7	59875.8	Georgia	70	*R*	488	*	Tan
ASV[a]	58723.8	58818.8	Serbia	140/60	*BVRI*	83	□	Black
Athens[b]	57736.6	58793.8	Greece	40	*R*	55	∘	Cyan
Belogradchik	59603.7	59872.0	Bulgaria	60	*VRI*	12	▽	Lime
Crimean (AP-7)	55401.0	59544.7	Russia	70	*BVRI*	1656	◁	Blue
Crimean (ST-7)	53516.0	59848.9	Russia	70	*BVRI*	1445	▷	Light sea-green
Hans Haffner	57280.8	60097.0	Germany	50	*BVR*	794	□	Red
KAO[c]	59576.7	59969.7	Egypt	188	*BVR*	174	△	Maroon
Lulin (SLT)	58251.8	60073.8	Taiwan	40	*VR*	824	▷	Indigo
MAPCAT[d]	59456.5	59938.3	Spain	220	*R*	14	◇	Gold
Perkins	55295.5	59930.1	United States	180	*BVRI*	1763	△	Green
Rozhen	55864.7	59107.7	Bulgaria	200	*BVRI*	185	⬠	Lime
Rozhen[e]	59581.7	59870.9	Bulgaria	50/70	*BVRI*	16	⬠	Lime
Siena	58380.9	58400.8	Italy	30	*R*	11	▽	Slate gray
Skinakas	56079.0	58709.9	Greece	130	*BVRI*	666	□	Lime
SNO[f]	59476.4	59958.3	Spain	90	*R*	127	⬡	Gold
St. Petersburg	53965.8	59901.7	Russia	40	*BVRI*	1101	⬡	Olive
Teide[g]	55669.5	60065.5	Spain	Various	*R*	330	+	Cyan
Tijarafe	57617.0	59952.8	Spain	40	*R*	924	x	Violet
SMARTS[h]	54662.3	57964.3	Chile	130/150	*BVR*	2178	∘	Tomato
Steward[i]	54745.2	58306.4	United States	154/230	*VR*	1101	+	Orange
WEBT[j]	53965.8	55543.8	International	Various	*BVRI*	15,017	◇	Purple
ZTF[k]	58254.4	59966.1	United States	122	*gr*	881	⬡	Maroon

Notes.
[a] Astronomical station Vidojevica.
[b] University of Athens Observatory (UOAO).
[c] Kottamia Astronomical Observatory.
[d] Calar ALTO Observatory.
[e] Rozhen 50/70 cm Schmidt telescope.
[f] Sierra Nevada Observatory.
[g] Teide Observatory with STELLA-I, IAC80, and Las Cumbres facilities.
[h] Small and Medium Aperture Research Telescope System with 130 and 150 cm telescopes.
[i] Steward Observatory Support of the Fermi Mission with 154 cm Kuiper and 230 cm Bok telescopes.
[j] Whole Earth Blazar Telescope Archive.
[k] Zwicky Transient Facility.

The FSRQ 3C 454.3, situated at a redshift of 0.859 (N. Jackson & I. W. A. Browne 1991), is one of the most rigorously monitored blazars over the whole EM spectrum on different timescales for the study of its various properties using flux, spectral, and polarization data (e.g., L. Fuhrmann et al. 2006; M. Villata et al. 2006, 2009; G. Ghisellini et al. 2007; C. M. Raiteri et al. 2007, 2008a, 2008b, 2011; A. A. Abdo et al. 2009; E. W. Bonning et al. 2009; S. G. Jorstad et al. 2010, 2013; M. Sasada et al. 2010, 2014; R. Bachev et al. 2011; P. M. Ogle et al. 2011; S. Vercellone et al. 2011; H. Gaur et al. 2012b; A. E. Wehrle et al. 2012; J. C. Isler et al. 2013; J. León-Tavares et al. 2013; A. C. Gupta et al. 2017; P. Kushwaha et al. 2017a; I. Villicaña-Pedraza et al. 2017; K. Nalewajko et al. 2019; A. Sarkar et al. 2019; R. A. Amaya-Almazán et al. 2021; J. H. Fan et al. 2021; N. Sahakyan 2021, and references therein). Following the launch of the `Fermi` satellite, it was identified as one of the most luminous γ-ray-emitting blazar (M. Ackermann et al. 2010). For this object, the mass of the supermassive black hole has been estimated to be in the range $(0.5–2.3) \times 10^9\, M_\odot$ (e.g., A. C. Gupta et al. 2017; K. Nalewajko et al. 2019, and references therein). This study focuses on the flux and color variability of FSRQ 3C 454.3, IDV analysis of the source on multiple nights in the *R* band, along with some of the long-term studies discussed in Section 3. The color or spectral variability studies provide insight into the currently dominant emission source, i.e., the jet or the AD, of the object under study. For the first time, the extensive observations of this source discussed here include multiple outbursts and quiescent phases, providing a rare opportunity to study the flux and color variations of a blazar over a long baseline of ∼20 yr.

In Section 2, we describe the extensive optical data we employ from many observatories around the world, along with archival data. In Section 3, we present our methods of analysis and findings related to IDV, STV, and LTV studies. Section 4 discusses our results from this extensive study with Section 5 summarizing our conclusions.

2. Observation and Data Processing

In the current work, observations of the FSRQ 3C 454.3 from many different telescopes across the globe made between 2004 June and 2023 June are combined. Some observation details are mentioned in Table 1. All the telescopes in Table 1

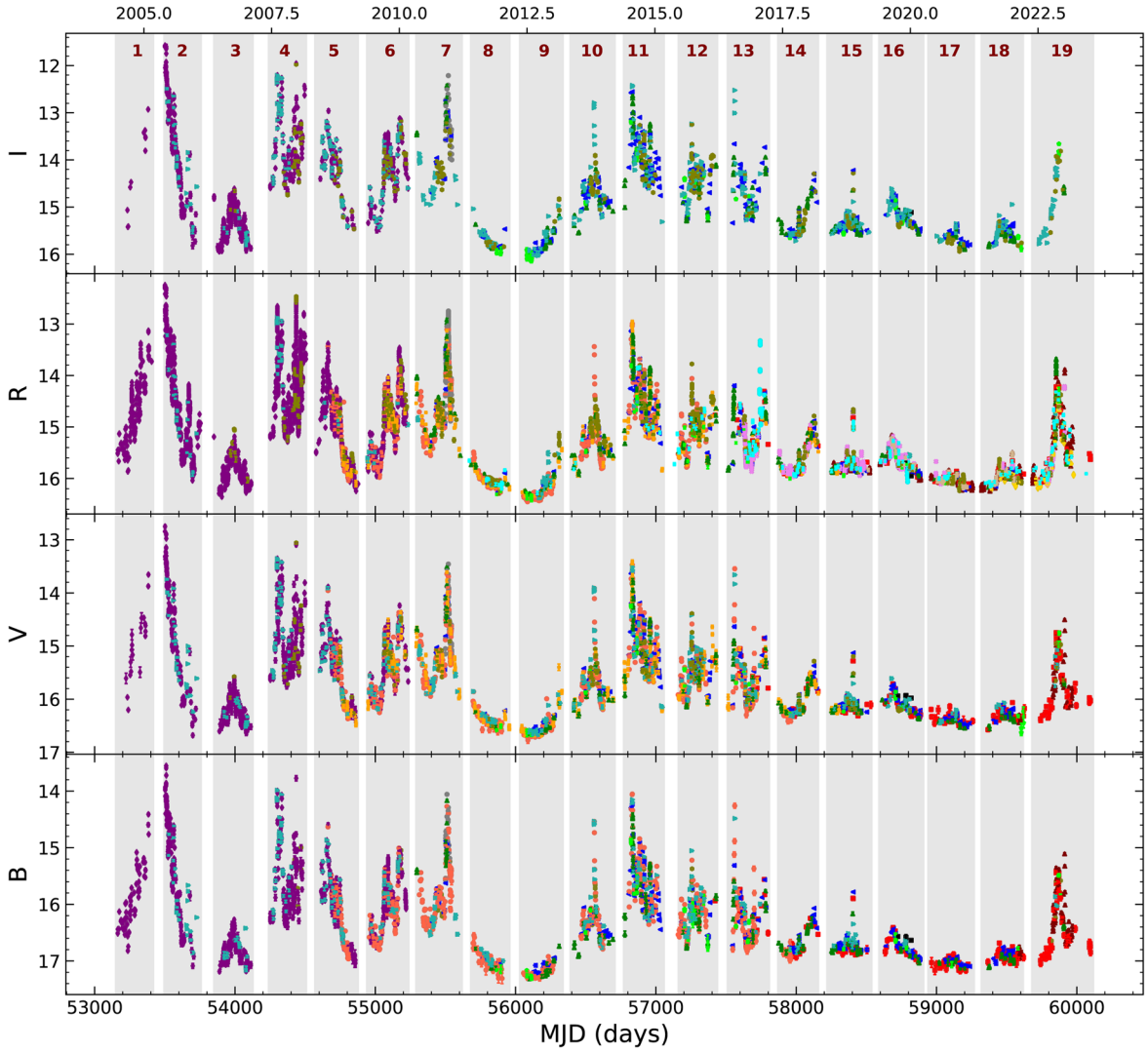

Figure 1. Extensively monitored optical LCs of the source in *BVRI* bands. The light curve consists of data from public archives and WEBT collaborators, identified by the colors given in Table 1.

utilize CCD detectors and broadband Johnson–Cousins filters (*UBVRI*); however, only the *BVRI* data are used in our analysis. Most of the data have been provided by the Whole Earth Blazar Telescope (WEBT[39]), which is an international team of observers who perform persistent optical-to-radio observations of a sample of γ-loud blazars, especially during phases of enhanced activity. WEBT data for this paper come both from the WEBT archive, containing results from past observing campaigns on the source (M. Villata et al. 2006, 2007, 2009; C. M. Raiteri et al. 2007, 2008a, 2008b, 2011; S. Vercellone et al. 2011), and from more recent observations by the teams listed in Table 1.

Data from public archives have also been incorporated. These are the Steward Observatory Support of the Fermi Mission (P. S. Smith et al. 2009; Steward[40]), Small and Medium Aperture Research Telescope System (SMARTS[41]; E. Bonning et al. 2012), and Zwicky Transient Facility (ZTF[42]) Observatory (E. C. Bellm et al. 2019). Steward Observatory provided data in the *V* and *R* filters, SMARTS in *B*, *V*, and *R* filters, and ZTF in *g* and *r* filters.

As shown in Figure 1, the entire light curve is divided into 19 segments (Seg) reflecting the gaps in observation cycles. As the light curve (LC) involves data from many telescopes around the globe, offset corrections are made if required. The WEBT archive data are taken as the reference for this as they are already offset-corrected. The optical photometry data from Steward, SMARTS, and ZTF observatories, along with unpublished data from current WEBT collaborators, are fully reduced and calibrated. The data are generally cleaned and reduced using the standard techniques discussed below. The first step is the cleaning of the raw image files using readily available techniques in Image Reduction and Analysis Facility (`IRAF`)[43] package. For this reduction, we make a master bias frame by median-combining all the bias frames using the `zero-combine` method for the individual night, which then is subtracted from science and flat-fielding images. After that,

[39] https://www.oato.inaf.it/blazars/webt/
[40] https://james.as.arizona.edu/~psmith/Fermi/
[41] http://www.astro.yale.edu/smarts/glast/home.php
[42] https://www.ztf.caltech.edu/ztf-public-releases.html

[43] IRAF is distributed by the National Optical Astronomy Observatories, which are operated by the Association of Universities for Research in Astronomy, Inc., under a cooperative agreement with the National Science Foundation.

Table 2
Short-term Segment-wise Variability Amplitudes of 3C 454.3

	Band	V_F		Band	V_F		Band	V_F		Band	V_F		Band	V_F		Band	V_F
	B	1.23		*B*	2.40		*B*	2.24		*B*	3.89		*B*	1.64		*B*	0.51
Seg	*V*	1.36	Seg	*V*	2.29	Seg	*V*	2.61	Seg	*V*	3.75	Seg	*V*	1.69	Seg	*V*	0.61
1	*R*	1.32	4	*R*	2.51	7	*R*	2.20	10	*R*	3.99	13	*R*	1.69	16	*R*	0.68
	I	1.49		*I*	2.31		*I*	2.82		*I*	4.17		*I*	1.75		*I*	0.87
	B	3.33		*B*	2.18		*B*	0.41		*B*	3.38		*B*	0.86		*B*	0.20
Seg	*V*	3.08	Seg	*V*	1.88	Seg	*V*	0.31	Seg	*V*	2.89	Seg	*V*	1.04	Seg	*V*	0.25
2	*R*	3.41	5	*R*	2.02	8	*R*	0.51	11	*R*	2.85	14	*R*	1.29	17	*R*	0.34
	I	3.53		*I*	1.99		*I*	0.52		*I*	2.88		*I*	1.68		*I*	0.53
	B	0.81		*B*	1.52		*B*	0.31		*B*	1.93		*B*	1.42		*B*	0.37
Seg	*V*	0.91	Seg	*V*	1.53	Seg	*V*	0.50	Seg	*V*	2.01	Seg	*V*	1.53	Seg	*V*	0.40
3	*R*	1.08	6	*R*	1.69	9	*R*	0.48	12	*R*	1.89	15	*R*	1.72	18	*R*	0.40
	I	1.25		*I*	1.87		*I*	0.58		*I*	2.55		*I*	2.02		*I*	0.56

the bias-subtracted flat frames from each night are median-combined using the `flatcombine` method to produce master flat frames for individual filters. These master flat frames are then used to normalize the science frames to remove pixel-to-pixel variations due to varying sensitivity and the presence of dust on filters and/or CCDs, or both. Next, cosmic-ray removal was carried out for the bias-subtracted and flat-fielded science frames using the `cosmicrays` package. After the cleaning process, the instrumental magnitudes of FSRQ 3C 454.3 and the standard stars are usually extracted using DAOPHOT[44] II (P. B. Stetson 1987, 1992) software using aperture photometry.

We performed aperture photometry on all the science frames using four concentric apertures with radii of 1, 2, 3, and 4 times the FWHM. Several studies (A. C. Gupta et al. 2016; A. Pandey et al. 2019) indicate that the signal-to-noise ratio is usually best for the aperture that is 2 times the FWHM, so we have generally employed it. The data reduction for the Bulgarian and Georgian telescopes is discussed by H. Gaur et al. (2012b) whereas A. Pandey et al. (2020) discuss the same for the Serbian telescopes.

For magnitude calibration and variability analysis, the standards[45] proposed by the GLAST-AGILE Support Program (GASP), i.e., stars 1, 2, 3, and 4, are observed in all science frames. Among these, star 4 has been used to calibrate the instrumental magnitudes of the source because its magnitude and color are closer to it, which reduces errors while performing differential photometry. Since all the standard stars and 3C 454.3 have been observed under the same weather conditions and air mass, there is no need to perform atmospheric extinction corrections.

3. Analysis Techniques and Results

The variability of an AGN over the broad EM spectrum is one of its defining characteristics. This variability is an excellent tool for probing the physical properties of the emission regions. Inspection of Figure 1 shows that 3C 454.3 is clearly variable over both long and short terms, and we compute the amplitude of variability during each segment. To investigate the presence of IDV for the blazar 3C 454.3, we have employed the enhanced F-test and nested analysis of variance (ANOVA) test techniques, which offer greater reliability than other widely used techniques such as the F-test. Discrete correlation function (DCF) analysis has been implemented to quantify any possible correlation among optical bands.

3.1. Amplitude Variation

For the light curves identified as being variable, we determined the amplitude of variation using the formula provided by J. Heidt & S. J. Wagner (1996):

$$V_F = \frac{\sqrt{(F_{\max} - F_{\min})^2 - 2\sigma^2}}{\bar{F}}. \quad (1)$$

Here $F_{\max}$, $F_{\min}$, and $\bar{F}$ are the highest, lowest, and mean fluxes of the variable light curve, with σ being the average error. The resulting STV amplitude variations in respective optical bands are shown in Table 2 for the first 18 segments. Segments 2, 10, and 11 are the most variable, while segments 16, 17, and 18 are the least variable across the entire light curve.

3.2. Color Variation and Model Selection

To study the spectral variation, we plotted diagrams of color index versus magnitude in Figure 2, in which data points are color coded according to which segment of the light curve contributed points to the CM diagram. The plots are arranged with increasing frequency differences between the bands (from top to bottom). All the plots indicate an RWB trend up to a cutoff magnitude (shown by a maroon vertical dashed line), although the trend is clearer and much more localized in the CM space when the bands are well separated, which can be understood in terms of the emission from the jet and the disk. The thermal part is mainly ascribed to the AD, whereas the nonthermal component arises from relativistic jet emissions. Nonetheless, a strict linear trend is not seen, as the color indices saturate at lower magnitudes (brighter phases), i.e., they increase more slowly and eventually flatten in the long term as the source brightens. This flattening was first noted by M. Villata et al. (2006).

To verify and quantify this, two functions have been fitted to all the plots in Figure 2, namely linear and piecewise, with their forms given below:

$$y = mx + c, \quad (2)$$

and

$$y_1 = m_1 x + c_1,$$
$$y_2 = m_2 x + c_2, \quad (3)$$

[44] Dominion Astronomical Observatory Photometry.
[45] https://www.oato.inaf.it/blazars/webt/3c-454-3-2251158/

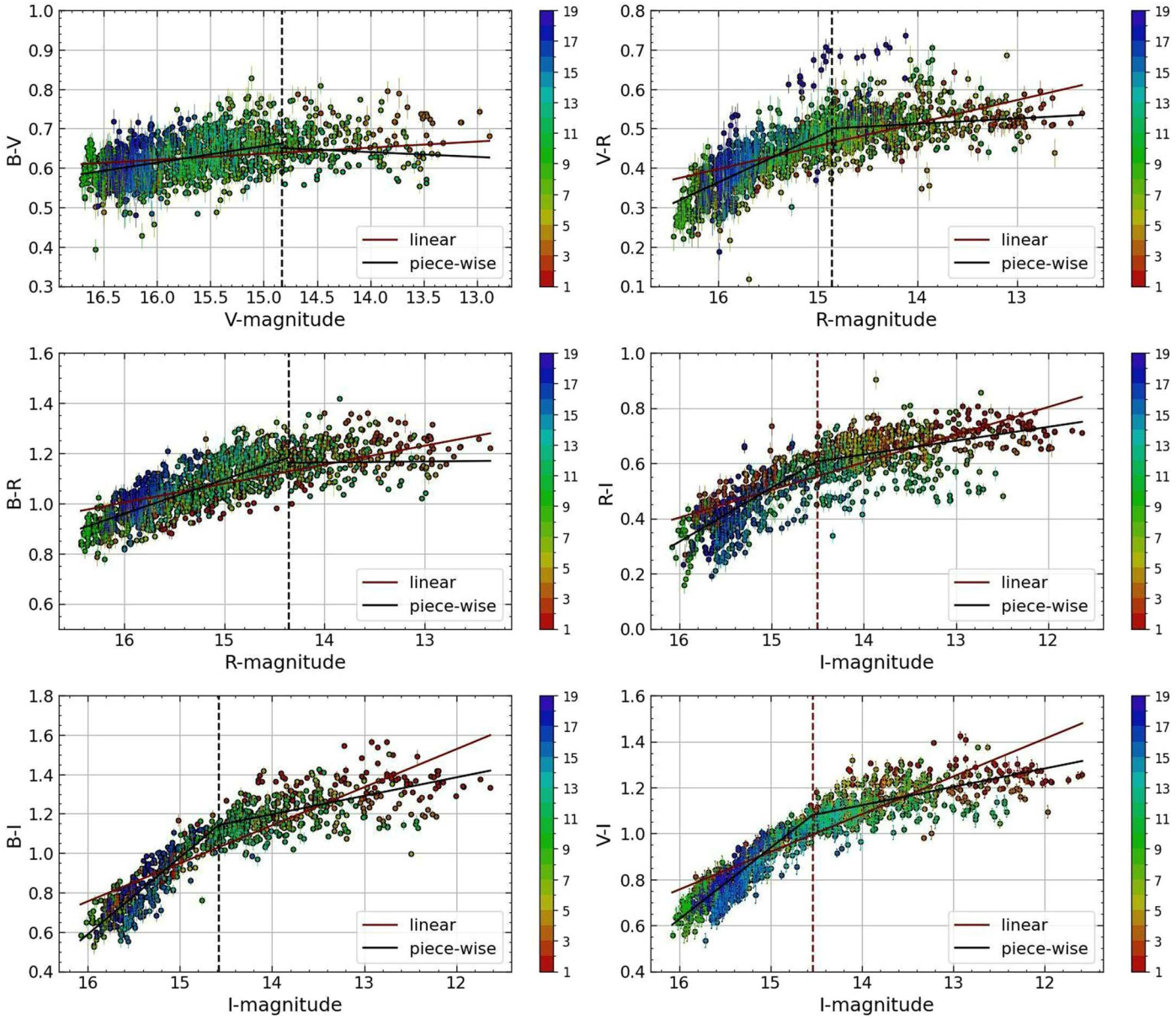

Figure 2. Plots of color index vs. magnitude.

where m is the slope of the line and c is the intercept. The parameters have been estimated using maximum likelihood estimation (MLE), which is implemented using the `emcee`[46] package. As the name suggests, MLE tries to maximize the likelihood function to get the best estimates of the parameters; however, maximizing the likelihood is similar to minimizing the negative logarithm of the likelihood, which brings an additional benefit, as the logarithm of the likelihood transforms the computations from multiplicative to summation series, which are much easier to work with. If the error bars are correct, Gaussian, and independent, the results of MLE would be the same as those of the simple least-squares methodology. Still, since those conditions do not necessarily apply, we can optimize the probability distribution function using MLE if we consider that the error bars are underestimated by some fractional amount. This correction makes our log-likelihood function become

$$\ln(L) = -\frac{1}{2}\sum_n \left[\frac{(y_n - mx_n - c)^2}{s_n^2} + \ln(2\pi s_n^2)\right]$$
$$\text{and } s_n^2 = \sigma^2 + f^2(mx + c)^2, \quad (4)$$

where f is the fractional amount by which variance is underestimated. If the errors assume a Gaussian distribution, f is set to zero. A Markov Chain Monte Carlo technique has been implemented to calculate the uncertainties in the evaluated parameters, which the MLE technique does not provide.

Now, to select between the models discussed above, Akaike's information criterion (AIC) and the Bayesian information criterion (BIC) have been calculated using the log-likelihood calculated previously. AIC and BIC are derived using frequentist and Bayesian approaches, respectively, and

[46] https://emcee.readthedocs.io/en/stable/

Table 3
Fitting Parameters for the Color–Magnitude Plots

Color versus Magnitude	Fitting Function	Slope and Break-point	Akaike's Information Criterion	Bayesian Information Criterion
$B-V$ versus V	Linear	slope $= -0.0154 \pm 0.0004$	18,501.78	18,512.71
	Piecewise linear	slope 1 $= -0.0417 \pm 0.0007$	16,386.47	16,408.33
		slope 2 $= 0.0121 \pm 0.0011$		
		break-point $= 14.833 \pm 0.007$		
$V-R$ versus R	Linear	slope $= -0.0583 \pm 0.0003$	16,864.10	16,875.24
	Piecewise linear	slope 1 $= -0.1164 \pm 0.0010$	8525.66	8547.93
		slope 2 $= -0.0136 \pm 0.0007$		
		break-point $= 14.862 \pm 0.010$		
$B-R$ versus R	Linear	slope $= -0.0756 \pm 0.0003$	52,233.52	52,244.38
	Piecewise linear	slope 1 $= -0.1363 \pm 0.0007$	38,710.39	38,732.10
		slope 2 $= -0.0037 \pm 0.0011$		
		break-point $= 14.362 \pm 0.016$		
$R-I$ versus I	Linear	slope $= -0.1002 \pm 0.0004$	22,229.64	22,239.80
	Piecewise linear	slope 1 $= -0.1954 \pm 0.0017$	13,553.37	13,573.71
		slope 2 $= -0.0500 \pm 0.0007$		
		break-point $= 14.509 \pm 0.015$		
$B-I$ versus I	Linear	slope $= -0.1933 \pm 0.0005$	49,477.65	49,487.39
	Piecewise linear	slope 1 $= -0.3904 \pm 0.0019$	23,843.73	23,863.22
		slope 2 $= -0.0937 \pm 0.0009$		
		break-point $= 14.577 \pm 0.012$		
$V-I$ versus I	Linear	slope $= -0.1639 \pm 0.0004$	34,557.59	34,567.89
	Piecewise linear	slope 1 $= -0.3107 \pm 0.0015$	13,133.09	13,153.70
		slope 2 $= -0.0797 \pm 0.0008$		
		break-point $= 14.538 \pm 0.007$		

are given by

$$\begin{aligned} \mathrm{AIC} &= 2k - 2\ln(L), \\ \mathrm{BIC} &= k\ln(n) - 2\ln(L), \end{aligned} \tag{5}$$

where k, n, and L represent the free parameters, data points, and likelihood function of the model, respectively. Both information criteria not only rely on how well the model fits the data but also consider the complexity of the respective fitting function. If we keep increasing the number of parameters in the model, the data will be overfitted—a problem both information criteria penalize—although this penalty is higher in BIC than AIC. The model with lower values of AIC and BIC is preferred. Piecewise linear functions fit the data better, as can be seen in Table 3; slope 1 and slope 2 represent the parts of the fit to the left and right of the break-point, respectively. In Figure 2, the maroon dashed lines indicate the break-points of the piecewise linear functions.

3.3. Power-enhanced F-test

To check the IDV of FSRQ 3C 454.3, we have implemented the power-enhanced F-test as described by J. A. de Diego (2014) and J. A. de Diego et al. (2015). This test has been widely used in recent variability studies (e.g., H. Gaur et al. 2015; J. Polednikova et al. 2016; S. K. Kshama et al. 2017; A. Pandey et al. 2019, 2020). In this test, the variance of the instrumental blazar differential light curve (DLC) is compared with the variances of the combined instrumental DLCs of comparison stars. The DLCs are produced with respect to a reference star. The comparison stars that do not show variability among themselves are considered. The reference star is the one whose magnitude is closest to the source's. The test statistics are given by

$$F = \frac{s_{\mathrm{blz}}^2}{s_c^2}, \tag{6}$$

where s_{blz}^2 is the variance of the target DLC, and s_c^2 is the combined variance of the DLCs of the comparison stars.

The value of s_c^2 is given by

$$s_c^2 = \frac{\sum_{j=1}^{k}\sum_{i=1}^{N_i} s_{j,i}^2}{(\sum_{j=1}^{k} N_j) - k}. \tag{7}$$

Here, N_j is the number of observations of the jth comparison star, and k is the number of comparison stars. The scaled square deviation of the jth comparison star is

$$s_{j,i}^2 = \omega_j (m_{j,i} - \bar{m}_j)^2, \tag{8}$$

where ω_j is the scaling factor, $m_{j,i}$ is the ith differential magnitude of the jth star, and $\bar{m}_j$ is the mean magnitude of the jth star. The scaling factor is defined as the ratio of the average square error of the blazar's DLC to the average square error of the jth comparison star's DLC.

During the observations, we observed six field stars, of which star 4 was chosen as the reference star, having the magnitude closest to the source. As we have the same number of observations (M) for field stars (q) and the source, the degrees of freedom (dof) for the numerator and denominator are $\nu_1 = M - 1$ and $\nu_2 = q(M-1)$, respectively. Along with the test statistic, which is the F-value, we need to calculate the critical F-value (F_c) along with the corresponding p-values. A comparison of F with F_c tells us about the significance of our

Table 4
Results of IDV Analysis for Nested ANOVA and Enhanced F-test

Obs. Date	Band	Enhanced F-test				Nested ANOVA Test				Status	V_F
yyyy-mm-dd		dof(ν_1, ν_2)	F_{enh}	F_c	p-value	dof(ν_1, ν_2)	F	F_c	p-value		(%)
2022-10-25	R	374, 1122	3.34	1.21	1.11×10^{-16}	14, 360	262.82	2.13	1.11×10^{-16}	V	7.33
2022-10-31	R	131, 524	10.94	1.36	1.11×10^{-16}	10, 121	208.60	2.47	1.11×10^{-16}	V	6.60
2022-11-14	R	434, 2170	2.52	1.18	1.11×10^{-16}	28, 406	24.71	1.77	1.11×10^{-16}	V	6.75
2022-12-21	R	164, 492	2.49	1.33	1.08×10^{-14}	14, 150	5.43	2.20	2.42×10^{-08}	V	16.41
2022-12-23	R	89, 267	3.25	1.47	8.44×10^{-14}	8, 81	7.38	2.74	2.50×10^{-07}	V	25.34
2022-12-25	R	155, 465	3.50	1.34	1.11×10^{-16}	12, 143	11.18	2.31	1.55×10^{-15}	V	14.11
2023-10-07	R	66, 198	0.54	1.56	0.997	10, 55	2.68	2.66	0.009	NV	⋯
2023-10-14	R	122, 366	0.64	1.39	0.998	10, 110	0.51	2.49	0.879	NV	⋯
2023-12-21	R	37, 111	0.22	1.8	0.999	8, 27	0.47	3.26	0.86	NV	⋯

result at that probability level, whereas the p-value indicates the probability of obtaining a result at least as extreme as the one observed, assuming the null hypothesis is correct. Using these parameters, we have calculated the enhanced F-test (F_{enh}) value with the critical F-value (F_c) at a confidence level of 99% or $\alpha = 0.01$. Only when $F_{enh} \geqslant F_c$ do we label the source as variable. The results are given in Table 4. The light curves found to be variable are marked as V, and the nonvariable ones are marked as NV. The amplitude of variability has also been computed for these LCs, with their results shown in the last column (V_F) of Table 4.

3.4. Nested ANOVA Test

An ANOVA test compares the means of different populations and checks whether the populations have intrinsic variation or are different. The nested ANOVA is a successor to the ANOVA test that further divides the groups into subgroups and then compares the means of these nested observations (J. A. de Diego et al. 1998, 2015). This test uses multiple field stars as a reference to produce the DLCs of the source. During the observations, we observed eight field stars, from which we took four to six reference stars (depending on the night) to generate DLCs of the blazar.

The test statistic, which is used to verify there is a significant difference between the group means, is given by

$$F = \frac{MS_G}{MS_{WG}}, \tag{9}$$

where MS_G represents the sum of squares (SS) average among groups and MS_{WG} represents the SS average due to nested observations. The formulae for MS_G and MS_{WG} are

$$MS_G = \sum_{i=1}^{n} \frac{(\bar{m_i} - \bar{m})^2}{r - 1};$$
$$MS_{WG} = \sum_{i=1}^{n}\sum_{j=1}^{n} \frac{(\bar{m_{ij}} - \bar{m_i})^2}{r(t-1)}. \tag{10}$$

Here, a and b represent the number of groups and the number of subgroups within a group, respectively. The F-ratio in Equation (9) follows the F-distribution with the numerator and denominator having $(r-1)$ and $r(t-1)$ degrees of freedom, respectively. If $F \geqslant F_c$, for $\alpha = 0.01$, then the source is taken to be variable, otherwise it is nonvariable. Only if both the nested ANOVA and enhanced F-test detect statistically significant variations do we consider the source to be variable on the IDV time span. The nested ANOVA test results are given in Table 4 with all the parameters already defined in the previous section. The first six light curves observed in the R band and shown in Figure 3 are found to be variable, whereas the last three are nonvariable, as confirmed by both the test statistics being lower than the critical value.

3.5. Discrete Correlation Function Analysis

The possible presence of different emission and absorbing regions around an AGN means that it is sometimes possible to find a time lag between different energy bands. Any time lag between different energy bands is usually investigated by calculating the DCF proposed by R. A. Edelson & J. H. Krolik (1988) and is generally used for data with irregular sampling. For a better estimation of errors associated with each bin, the method was further improved by B. R. Hufnagel & J. N. Bregman (1992). A positive DCF value indicates a possible positive correlation, whereas a DCF value of less than zero indicates an anticorrelation between the bands. Figure 4 shows DCF plots between different optical bands. The maximum in each DCF plot is shown by a red vertical dashed line, which lies at zero lag for all the plots. As there is no significant lag between the different band combinations, the optical emission can be taken to arise from a single region.

3.6. Spectral Variation

To study any variability of the optical spectrum, we used the fluxes in different filters and plotted the fluxes in these bands over the whole time series, yielding around 972 quasi-simultaneous (within 1 day) data points. Figure 5 shows some spectra at different times with straight lines showing the least-squares fits to the data points. The plots of specific flux versus frequency shown in Figure 5 are in logarithmic space and follow $F_\nu \propto \nu^{-\alpha}$, where the slopes of the least-squares fits give optical spectral indices. To correct for Galactic extinction, we subtracted the extinction correction values (taken from NASA's Extragalactic Database, NED) of the respective band from our observations. The extinction corrections for the B, V, R, and I bands are 0.382, 0.289, 0.228, and 0.159, respectively. We used Vega as our standard star to convert calibrated magnitudes to flux values, which are given in SI units. A temporal evolution of the fluxes in different bands has been generated with all the data points with a subset shown in Figure 5.

Figure 6 shows the distribution of spectral indices, here defined as the slopes of the spectra shown in Figure 5. This reveals a bimodal distribution, with the number of bins taken to be 34, and we fitted it using two Gaussian distributions, with their parameters given in Table 5. The two Gaussian fits are

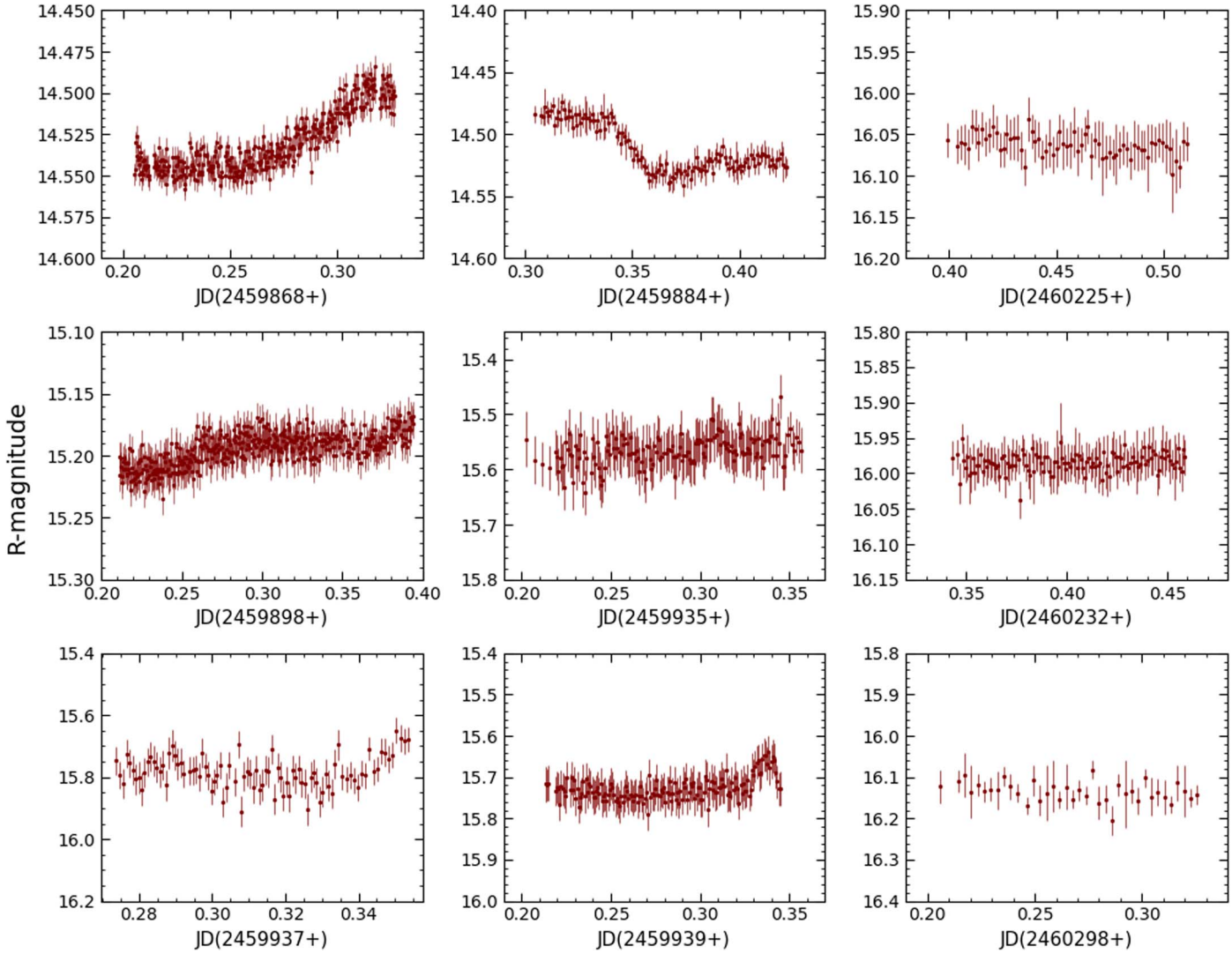

Figure 3. Intraday LCs of FSRQ 3C 454.3 in the *R* filter for 9 days. Each plot shows the respective date (in JD on the *x*-axis) on which observation is taken.

shown by red dashed lines, and their combined fit is illustrated using a solid red line. This bimodal nature indicates the presence of two common phases for the states of 3C 454.3, i.e., a bright/outburst phase and a faint/quiescent phase, with the former contributing to the first hump and the latter contributing to the second hump of the bimodal distribution.

4. Discussion

In this study, the optical photometric data of FSRQ 3C 454.3 collected for over 20 yr have been analyzed. The data have been collected from the WEBT archive and its collaborators and include both new and published observations along with data from other public archives such as SMARTS, Steward, and ZTF. During this long observation period, the object underwent a drastic change in its magnitude in most observing seasons, as shown in Figure 1. The exceptions are segments 7, 8, 16, 17, and 18, which have a maximum change in magnitude of ∼0.5 mag compared to 11 other segments, evincing a minimum change of ∼1 mag and reaching a maximum change of ∼4 mag in the *R* band in segment 8 and segment 2 respectively. As can be seen in Table 2, the longer wavelength bands are more variable than the shorter ones. This can be explained by considering that synchrotron emission is more variable than disk emission, and given that disk emission peaks in the near-UV, it will make smaller contributions toward longer wavelengths, and hence the variability will be strongest in the longer wavelength regime. The diverse flux variability this blazar shows may be explained by fluctuations in the jet, along with the presence of the disk instabilities. For instance, the shock-in-jet model, in which internal shocks move along the jet, can explain the variability over diverse timescales (A. P. Marscher & W. K. Gear 1985; S. J. Wagner & A. Witzel 1995; M. Spada et al. 2001). Some of the faster and small-scale amplitude variations can result from various instabilities in the AD (P. J. Wiita et al. 1992; S. K. Chakrabarti & P. J. Wiita 1993). Geometrical effects (e.g., M. Camenzind & M. Krockenberger 1992) can also explain IDV (S. J. Wagner & A. Witzel 1995) and the LTV via the production of fluctuations in the value of the Doppler factor that can result from changes in our line of sight to the predominant emission region in an inhomogeneous, curved, or twisting jet (Gopal-Krishna & P. J. Wiita 1992; M. Villata & C. M. Raiteri 1999; C. M. Raiteri et al. 2017) along with misalignment of AGN jets (A. K. Singal 2016). Another scenario that can be responsible for jet fluctuations, especially during flaring events, involves the

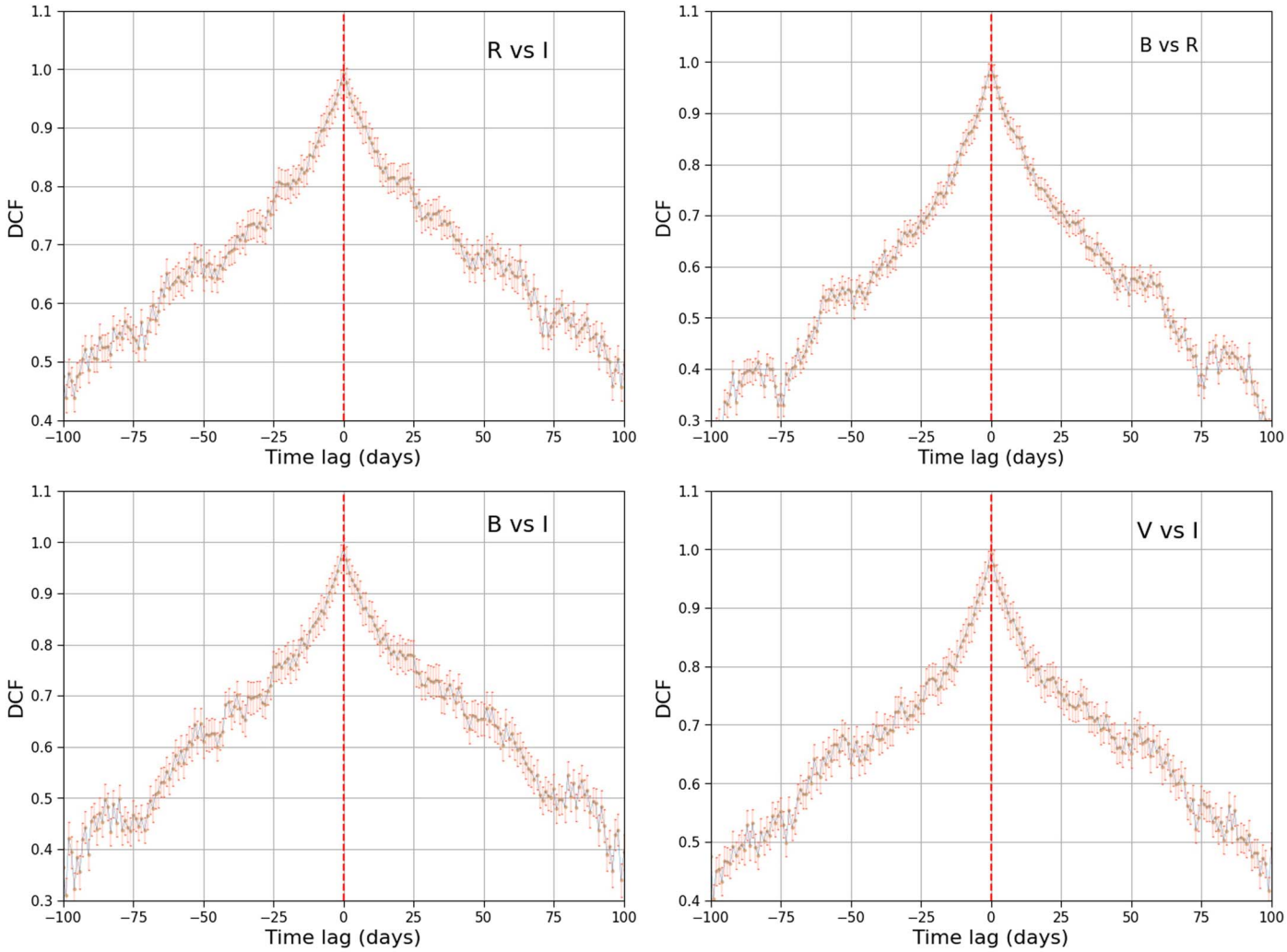

Figure 4. DCF plots for the entire observation period (here shown for 100 days lag) between different pairs of wave bands.

collision of a blob with a quasi-stationary jet component (R. A. Amaya-Almazán et al. 2021).

The BWB trend observed in BL Lac objects can be explained by the fact that electrons accelerated by the shock front in the jet dissipate energy more rapidly, causing the higher energy bands to be more variable (A. Mastichiadis & J. G. Kirk 2002). Alternatively, the increase in luminosity could be explained by the introduction of new electrons with a harder energy distribution than the previously cooled ones. On the other hand, in the case of FSRQs, the RWB trend can be simply explained by adding the redder jet emission to the bluer disk emission (M. F. Gu et al. 2006; J. C. Isler et al. 2017), provided jet emission has not swamped the disk emission.

In this paper, the long-term color variability was studied using different pairs of color versus magnitude plots, which revealed a variety of CM trends through which the object evolved. FSRQ 3C 454.3 has a bright AD, and its multi-wavelength SED is well fitted using the external Compton model (A. E. Wehrle et al. 2012), which tells us about the presence of soft photons from the broad-line-emitting region and the dusty torus region. For the object under study, the major emission feature appearing in the spectra is the Mg II line (K. Nalewajko et al. 2019), which falls at 5200 Å in the observer's frame, between the B and V bands. Due to the usage of broadband Johnson–Cousins $BVRI$ filters, the intensity of the line is smeared out in the photometric observations and does not contribute significantly to the object's color. Another study, conducted by J. Acosta-Pulido et al. (2017), reveals that in bright phases of the source, the contribution of the Mg II line on top of the continuum becomes negligible.

However, since the line does not vary with the same intensity as the continuum, it is worth examining whether the Mg II line will influence the $B-V$ color in the low-activity phases. We assume a correlation between the Mg II line and continuum flux for simplicity and that Mg II primarily influences the V-band magnitude, and based on the continuum and Mg II line flux retrieved from Figure 1 of K. Nalewajko et al. (2019), we found that the $B-V$ color difference between maximum and minimum continuum flux states, excluding the Mg II contribution, is only 0.25% larger than that difference when the Mg II contribution is included. While this estimate may have limitations, it offers a scale for the Mg II line's impact on the $B-V$ color. Given that the $B-V$ colors in this work range from 0.4 to 0.8, this ∼0.25% difference amounts to ∼0.01–0.02 and does not significantly alter our following analysis. We can conclude that only two major components dictate the path of the CM plot, i.e., the jet and the disk emission. Owing to the abundance of nearly simultaneous data points in our study, the interplay of these two components can be nicely seen in Figure 6 with two well-separated humps,

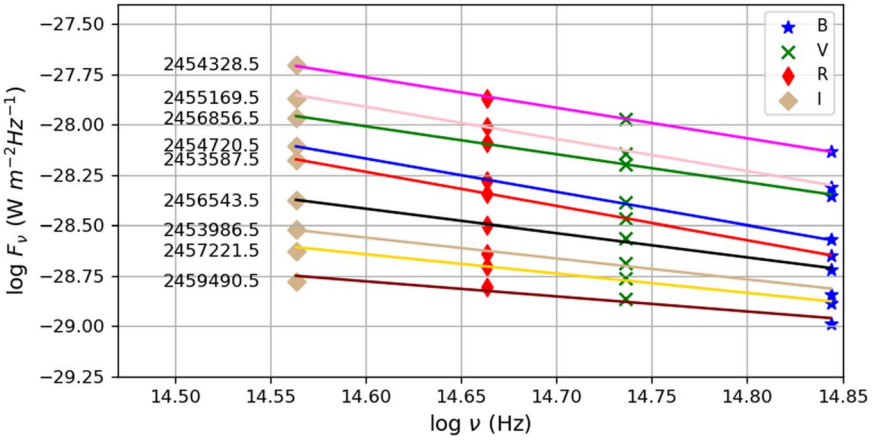

Figure 5. A still image showing nine different spectral indices from the associated animation. The corresponding Julian dates are shown on the left side, with the legend showing the corresponding band/filter used. The animation runs for a total of 39 s and shows the variation of optical spectral indices over the whole observation period of 19 yr. The animation provides a visualization of the variation of spectral indices through which the source evolves and shows a nice bimodal distribution that correlates with the high and low states of the source.
(An animation of this figure is available.)

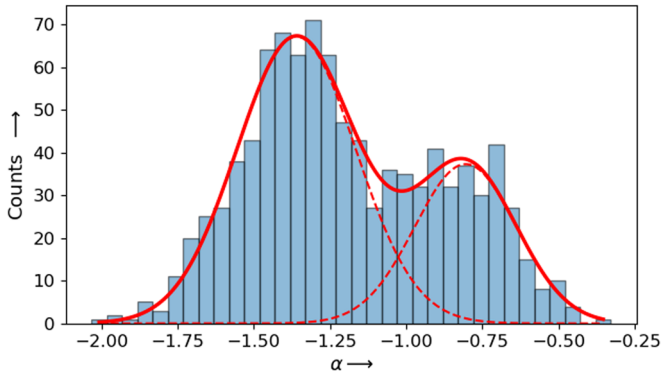

Figure 6. Distribution of spectral indices.

Table 5
Values of the Bimodal Fit to the Spectral Index Distribution

	μ_1	σ_1	A_1	μ_2	σ_2	A_2
Value	−1.362	0.192	67.430	−0.808	0.169	37.541
Error	0.011	0.012	2.413	0.016	0.019	2.567

Note. μ, σ, and A represent the mean, standard deviation, and amplitude, respectively.

peaking at spectral index values of ∼−1.36 and ∼−0.81, respectively. The first and the second humps correlate with the bright and faint states of the object, indicating that 3C 454.3 was more commonly in bright phases throughout the observation period. The tail part of the second hump of the bimodal distribution approaches zero but is never positive, implying that even in the faintest state of the source, the jet component is present, i.e., the disk emission never entirely swamped the jet emission in any segment.

The RWB trend indicates that disk emission is more prominent during the object's low-flux or quiescent stages (R. A. Amaya-Almazán et al. 2021), and jet emission dominates in higher-flux stages. This can be supported by the fact that the object under study is an FSRQ, which is an LSP blazar; hence its first hump peak lies around the IR band, which implies that in the optical regime, the jet emission is *"redder"* in nature, i.e., flux decreases with increasing frequency. On the other hand, the disk emission for black hole masses $\gtrsim 10^8\,M_\odot$ peaks in the UV band; as a result, disk emission will be *"bluer"* in nature, i.e., the flux increases with increasing frequency in the optical regime. Hence, the overall result of the RWB trend indicates that, with increasing brightness, the jet emission indeed dominates. Nonetheless, the peak synchrotron frequency need not remain the same over such a long observation period. For example, when the jet emission is weak compared to that of the disk, the synchrotron peak frequency can be lower (R. Chatterjee et al. 2013). This can cause the spectrum to be much steeper in the optical regime, thereby reducing the redder contribution, which, in effect, will cause the object to be bluer during such a phase.

One of the studies conducted by E. Bonning et al. (2012) using SMARTS data included 3C 454.3 as a target, and they found that the object followed an RWB trend throughout the observation campaign of ∼2.5 yr. Another study having 3C 454.3 in the target list, conducted by P. Z. Safna et al. (2020), found that it displayed RWB behavior throughout the observation campaign of ∼9 yr. Although their plot revealed deviations toward the brighter end, the lack of sufficient data points in the bright state of the object meant they could only fit it using a straight line.

Our long-term study reveals that it is not possible to simply classify this blazar (and probably many others) as RWB or BWB. Rather, the behavior seems to depend on the specific nature of the plasma ejections, the possible interaction of a blob with the quasi-stationary jet component, and other physical processes discussed below, assuming the disk emission varies slowly compared to the highly fluctuating jet emission. When the jet is in the quiescent phase, or the jet emission has not outshone the disk emission, the objects trace a localized path on the CM diagram, remaining in the RWB/bluer-when-fainter state. But this localization continues only up to a particular magnitude value, shown by a vertical dashed line in Figure 2, after which the color plot saturates/flattens and then can redden or become bluer or merely achromatic, which in turn relies upon the processes mentioned above that are causing the increase in brightness of the source. The flattening that occurs at the break-point results from the canceling of the relative emissions of the jet and the disk, i.e., when their contributions

become equal, which is different from the achromatic behavior observed during the bright phases of the object. Up to the point where the RWB trend is strictly followed over the long term, the break-point indicates a crude magnitude value, after which the jet emission completely outshines the disk emission. The RWB continuing after the break-point may be attributed to different electron acceleration events rather than merely an admixture of disk and jet emissions, as the disk component has already been swamped by the jet, signatures of which can be seen in Figure 2 after the cutoff magnitude. This can happen if the new population of relativistic plasma does not extend as high up in energy as previously cooled ones, causing the spectrum to become softer. The achromatic behavior after jet emission has swamped the disk emission can be explained using diffusive/escape cooling (J. C. Isler et al. 2017). If the electron population escapes the emission region much faster (being energy-dependent, high-energy electrons will leave faster) before they can efficiently radiate, they will not contribute to the CM plot, causing the object to evolve achromatically in the CM plot. Apart from this, if there is a change in the jet direction and the wave bands get Doppler-boosted or deboosted equally, the blazar will become brighter or fainter, respectively, without any change in the CM plot, provided the spectrum maintains its slope in the Doppler-boosted wave bands.

Thus, the evolution of the CM plot as a source brightens should be treated as a continuous transition from the mixture of jet and disk colors until it flattens and then evolves to BWB, RWB, and achromatic state depending upon the processes involved that are causing the change in brightness. This again goes back to disk and jet contributions as the object moves from a bright to a faint state. In effect, the results from previous studies may be regarded as *"fragments"* of the whole CM plot depending upon the epoch in which the observation occurred. To get the fuller picture, long-term observations with a large number of quasi-simultaneous data points, in both bright and faint states, as we have here for 3C 454.3, are required to properly determine the CM behavior and evolution of other blazars.

5. Conclusions

The present work provides the most extensive and densely sampled long-term optical photometric variability studies of the FSRQ blazar 3C 454.3. The data used here were collected from a large number of ground-based optical telescopes around the globe between 2004 and 2023. Below is a summary of our findings.

1. During this lengthy period, this blazar was found to be highly variable, with a change of ∼5 mag in all four (*BVRI*) optical bands. 3C 454.3 was observed in various flux states: low states, pre- and post-outburst states, and outburst states on multiple occasions. We divided the total light curve into 19 segments based on the observing season. The minimum and maximum variability amplitudes in a given segment were respectively found to be 0.20 mag in the *B* band in segment 17 and 4.17 mag in the *I* band in segment 10.
2. We studied IDV in the *R* band for this blazar during nine nights when dense observations were available using the nested ANOVA and enhanced F-test. The object was variable on the intraday timescale during six of those nights, as confirmed by the combined results of both tests.
3. The various color versus magnitude combinations seen in the entire data sets of the *BVRI*-band light curves show clear evidence of an RWB trend, a well-established color versus magnitude trend in FSRQs, but only up to a certain magnitude value. Beyond that magnitude, the CM plot shows saturation and then evolves in a complex fashion, going through BWB, RWB, or achromatic states. These variations may depend on the energetics of the electron population that is causing the change in brightness. Our analysis reveals that it is possible to extract the magnitude value at which jet emission completely outshines the disk emission using an optical CM plot, which is ∼14.5 in the *I* band for 3C 454.3, provided sufficient long-term observations are present with a good number of quasi-simultaneous data points in different bands.
4. We performed cross-correlation analyses in different optical bands for the whole duration of the light curves using the DCF analysis method. The DCF plots in different optical bands all peak at zero lag, indicating that the emission is cospatial in the *BVRI* optical bands.
5. We also generated multiepoch extinction-corrected optical SEDs for the entire duration of these observations to search for spectral evolution. The optical SEDs are well fitted by power laws, and we estimated the spectral indices at different epochs during those two decades. The spectral indices exhibit a bimodal distribution, reflecting the presence of phases when the jet is more dominant or relatively quiescent.

Acknowledgments

Based on data taken and assembled by the WEBT collaboration and stored in the WEBT archive at the Osservatorio Astrofisico di Torino—INAF (https://www.oato.inaf.it/blazars/webt/). This study was based in part on observations conducted using the 1.8 m Perkins Telescope Observatory (PTO) in Arizona, which is owned and operated by Boston University. This paper has made use of up-to-date SMARTS optical/near-infrared light curves that are available at http://www.astro.yale.edu/smarts/glast/home.php. Data from the Steward Observatory spectropolarimetric monitoring project were used. This program is supported by Fermi Guest Investigator grants NNX08AW56G, NNX09AU10G, NNX12AO93G, and NNX15AU81G. The ZTF survey is supported by the U.S. National Science Foundation under grants No. AST-1440341 and AST-2034437. The Skinakas Observatory is a collaborative project of the University of Crete, the Foundation for Research and Technology–Hellas, and the Max-Planck-Institut für Extraterrestrische Physik. This article is partly based on observations made with the IAC80, the STELLA, and the LCOGT 0.4 m telescopes. The IAC80 telescope is operated by the Instituto de Astrofísica de Canarias in the Spanish Observatorio del Teide on the island of Tenerife. Many thanks are due to the IAC support astronomers and telescope operators for supporting the observations at the IAC80 telescope. The STELLA robotic telescopes are an AIP facility jointly operated by AIP and IAC. One of the nodes of the LCOGT 0.4 m telescope network is located in the Spanish Observatorio del Teide.

C.M.R., M.V., and M.I.C. acknowledge financial support from the INAF Fundamental Research Funding Call 2023. The research at Boston University was supported in part by several NASA Fermi Guest Investigator grants; the latest are 80NSSC22K1571 and 80NSSC23K1507. R.B., E.S., and A. S. were partially supported by the Bulgarian National Science Fund of the Ministry of Education and Science under grant KP-06-H68/4 (2022). G.D., O.V., M.D.J., and M.S. acknowledge support from the Astronomical station Vidojevica, funding from the Ministry of Science, Technological Development and Innovation of the Republic of Serbia (contract No. 451-03-66/2024-03/200002), by the EC through project BELISSIMA (call FP7-REGPOT-2010-5, No. 256772), the observing and financial grant support from the Institute of Astronomy and Rozhen NAO BAS through the bilateral SANU-BAN joint research project "GAIA astrometry and fast variable astronomical objects," and support by the SANU project F-187. Also, this research was supported by the Science Fund of the Republic of Serbia, grant No. 6775, Urban Observatory of Belgrade—UrbObsBel. NRIAG team acknowledges financial support from the Egyptian Science, Technology & Innovation Funding Authority (STDF) under grant No. 45779. The *R*-band photometric data from the University of Athens Observatory (UOAO) were obtained in the frame of *BOSS Project* after utilizing the robotic and remotely controlled instruments at the University of Athens (K. Gazeas 2016). The IAA-CSIC coauthors acknowledge financial support from the Spanish "Ministerio de Ciencia e Innovación" (MCIN/AEI/10.13039/501100011033) through the Center of Excellence Severo Ochoa award for the Instituto de Astrofísica de Andalucía-CSIC (CEX2021-001131-S), and through grants PID2019-107847RB-C44 and PID2022-139117NB-C44. Some of the data are based on observations collected at the Observatorio de Sierra Nevada, which is owned and operated by the Instituto de Astrofísica de Andalucía (IAA-CSIC), and at the Centro Astronómico Hispano en Andalucía (CAHA); which is operated jointly by Junta de Andalucía and Consejo Superior de Investigaciones Científicas (IAA-CSIC). L.C. acknowledges the support from the Tianshan Talent Training Program (grant No. 2023TSYCCX0099). M.F.G. is supported by the National Science Foundation of China (grant 12473019), the China Manned Space Project with No. CMSCSST-2021-A06, the National SKA Program of China (grant No. 2022SKA0120102), and the Shanghai Pilot Program for Basic Research–Chinese Academy of Science, Shanghai Branch (JCYJ-SHFY-2021-013). Z.Z. is funded by the National Science Foundation of China (grant No. 12233005).

ORCID iDs

Karan Dogra https://orcid.org/0009-0007-3214-602X
Alok C. Gupta https://orcid.org/0000-0002-9331-4388
C. M. Raiteri https://orcid.org/0000-0003-1784-2784
M. Villata https://orcid.org/0000-0003-1743-6946
Paul J. Wiita https://orcid.org/0000-0002-1029-3746
S. O. Kurtanidze https://orcid.org/0000-0002-0319-5873
S. G. Jorstad https://orcid.org/0000-0001-6158-1708
R. Bachev https://orcid.org/0000-0002-0766-864X
G. Damljanovic https://orcid.org/0000-0002-6710-6868
S. S. Savchenko https://orcid.org/0000-0003-4147-3851
O. Vince https://orcid.org/0009-0008-5761-3701
J. A. Acosta-Pulido https://orcid.org/0000-0002-0433-9656
I. Agudo https://orcid.org/0000-0002-3777-6182
G. Andreuzzi https://orcid.org/0000-0001-5125-6397
D. A. Blinov https://orcid.org/0000-0003-0611-5784
G. A. Borman https://orcid.org/0000-0002-7262-6710
M. I. Carnerero https://orcid.org/0000-0001-5843-5515
D. Carosati https://orcid.org/0000-0001-5252-1068
W. P. Chen https://orcid.org/0000-0003-0262-272X
Lang Cui https://orcid.org/0000-0003-0721-5509
E. G. Elhosseiny https://orcid.org/0000-0002-9751-8089
K. Gazeas https://orcid.org/0000-0002-8855-3923
Minfeng Gu https://orcid.org/0000-0002-4455-6946
R. Z. Ivanidze https://orcid.org/0009-0005-7297-8985
M. D. Jovanovic https://orcid.org/0000-0003-4298-3247
G. N. Kimeridze https://orcid.org/0000-0002-5684-2114
O. M. Kurtanidze https://orcid.org/0000-0001-5385-0576
M. Liao https://orcid.org/0000-0002-9137-7019
A. Marchini https://orcid.org/0000-0003-3779-6762
C. Marinelli https://orcid.org/0000-0002-3596-4307
A. P. Marscher https://orcid.org/0000-0001-7396-3332
M. G. Nikolashvili https://orcid.org/0000-0003-0408-7177
E. Semkov https://orcid.org/0000-0002-1839-3936
L. A. Sigua https://orcid.org/0000-0002-6985-2143
M. Stojanovic https://orcid.org/0000-0002-4105-7113
A. Takey https://orcid.org/0000-0003-1423-5516
Amira A. Tawfeek https://orcid.org/0000-0002-8279-9236
An-Li Tsai https://orcid.org/0000-0002-3211-4219
K. Vrontaki https://orcid.org/0009-0002-7669-7425
Zhongli Zhang https://orcid.org/0000-0002-8366-3373
Wenwen Zuo https://orcid.org/0000-0002-4521-6281

References

Abdo, A. A., Ackermann, M., Agudo, I., et al. 2010, ApJ, 716, 30
Abdo, A. A., Ackermann, M., Ajello, M., et al. 2009, ApJ, 699, 817
Ackermann, M., Ajello, M., Baldini, L., et al. 2010, ApJ, 721, 1383
Acosta-Pulido, J., Castro Segura, N., Carnerero, M., & Raiteri, C. 2017, Galax, 5, 1
Agarwal, A., Gupta, A. C., Bachev, R., et al. 2015, MNRAS, 451, 3882
Amaya-Almazán, R. A., Chavushyan, V., & Patiño-Álvarez, V. M. 2021, ApJ, 906, 5
Antonucci, R., & Barvainis, R. 1990, ApJL, 363, L17
Bachev, R., Semkov, E., Strigachev, A., et al. 2011, A&A, 528, L10
Barvainis, R. 1993, ApJ, 412, 513
Bellm, E. C., Kulkarni, S. R., Graham, M. J., et al. 2019, PASP, 131, 018002
Blandford, R. D., & Rees, M. J. 1978, PhyS, 17, 265
Bonning, E., Urry, C. M., Bailyn, C., et al. 2012, ApJ, 756, 13
Bonning, E. W., Bailyn, C., Urry, C. M., et al. 2009, ApJL, 697, L81
Böttcher, M. 2007, Ap&SS, 309, 95
Bregman, J. N. 1990, A&ARv, 2, 125
Camenzind, M., & Krockenberger, M. 1992, A&A, 255, 59
Chakrabarti, S. K., & Wiita, P. J. 1993, ApJ, 411, 602
Chatterjee, R., Fossati, G., Urry, C. M., et al. 2013, ApJL, 763, L11
Collin-Souffrin, S., Czerny, B., Dumont, A. M., & Zycki, P. T. 1996, A&A, 314, 393
Czerny, B., & Elvis, M. 1987, ApJ, 321, 305
de Diego, J. A. 2014, AJ, 148, 93
de Diego, J. A., Dultzin-Hacyan, D., Ramírez, A., & Benítez, E. 1998, ApJ, 501, 69
de Diego, J. A., Polednikova, J., Bongiovanni, A., et al. 2015, AJ, 150, 44
Dhiman, V., Gupta, A. C., Bachev, R., et al. 2024, MNRAS, 527, 1344
Edelson, R. A., & Krolik, J. H. 1988, ApJ, 333, 646
Fan, J. H., Kurtanidze, S. O., Liu, Y., et al. 2021, ApJS, 253, 10
Ferland, G. J., Korista, K. T., & Peterson, B. M. 1990, ApJL, 363, L21
Fossati, G., Maraschi, L., Celotti, A., Comastri, A., & Ghisellini, G. 1998, MNRAS, 299, 433
Fuhrmann, L., Cucchiara, A., Marchili, N., et al. 2006, A&A, 445, L1
Gaur, H., Gupta, A. C., Bachev, R., et al. 2015, MNRAS, 452, 4263
Gaur, H., Gupta, A. C., Strigachev, A., et al. 2012a, MNRAS, 425, 3002
Gaur, H., Gupta, A. C., & Wiita, P. J. 2012b, AJ, 143, 23
Gazeas, K. 2016, RMxAC, 48, 22
Ghisellini, G., Foschini, L., Tavecchio, F., & Pian, E. 2007, MNRAS, 382, L82

Ghisellini, G., Villata, M., Raiteri, C. M., et al. 1997, A&A, 327, 61
Gopal-Krishna, & Wiita, P. J. 1992, A&A, 259, 109
Gu, M., & Ai, Y. L. 2011, JApA, 32, 87
Gu, M. F., Lee, C. U., Pak, S., Yim, H. S., & Fletcher, A. B. 2006, A&A, 450, 39
Gupta, A. C., Agarwal, A., Bhagwan, J., et al. 2016, MNRAS, 458, 1127
Gupta, A. C., Banerjee, D. P. K., Ashok, N. M., & Joshi, U. C. 2004, A&A, 422, 505
Gupta, A. C., Mangalam, A., Wiita, P. J., et al. 2017, MNRAS, 472, 788
Heidt, J., & Wagner, S. J. 1996, A&A, 305, 42
Hufnagel, B. R., & Bregman, J. N. 1992, ApJ, 386, 473
Isler, J. C., Urry, C. M., Coppi, P., et al. 2013, ApJ, 779, 100
Isler, J. C., Urry, C. M., Coppi, P., et al. 2017, ApJ, 844, 107
Jackson, N., & Browne, I. W. A. 1991, MNRAS, 250, 414
Jorstad, S. G., Marscher, A. P., Larionov, V. M., et al. 2010, ApJ, 715, 362
Jorstad, S. G., Marscher, A. P., Smith, P. S., et al. 2013, ApJ, 773, 147
Kshama, S. K., Paliya, V. S., & Stalin, C. S. 2017, MNRAS, 466, 2679
Kushwaha, P., Gupta, A. C., Misra, R., & Singh, K. P. 2017a, MNRAS, 464, 2046
Kushwaha, P., Sinha, A., Misra, R., Singh, K. P., & de Gouveia Dal Pino, E. M. 2017b, ApJ, 849, 138
Laor, A., & Netzer, H. 1989, MNRAS, 238, 897
León-Tavares, J., Chavushyan, V., Patiño-Álvarez, V., et al. 2013, ApJL, 763, L36
Malkan, M. A., & Sargent, W. L. W. 1982, ApJ, 254, 22
Marcha, M. J. M., Browne, I. W. A., Impey, C. D., & Smith, P. S. 1996, MNRAS, 281, 425
Marscher, A. P., & Gear, W. K. 1985, ApJ, 298, 114
Mastichiadis, A., & Kirk, J. G. 2002, PASA, 19, 138
Miller, H. R., Carini, M. T., & Goodrich, B. D. 1989, Natur, 337, 627
Mücke, A., Protheroe, R. J., Engel, R., Rachen, J. P., & Stanev, T. 2003, APh, 18, 593
Nalewajko, K., Gupta, A. C., Liao, M., et al. 2019, A&A, 631, A4
Ogle, P. M., Wehrle, A. E., Balonek, T., & Gurwell, M. A. 2011, ApJS, 195, 19
Pandey, A., Gupta, A. C., Damljanovic, G., et al. 2020, MNRAS, 496, 1430
Pandey, A., Gupta, A. C., Wiita, P. J., & Tiwari, S. N. 2019, ApJ, 871, 192
Polednikova, J., Ederoclite, A., de Diego, J. A., et al. 2016, MNRAS, 460, 3950
Raiteri, C. M., Villata, M., Acosta-Pulido, J. A., et al. 2017, Natur, 552, 374
Raiteri, C. M., Villata, M., Aller, M. F., et al. 2011, A&A, 534, A87
Raiteri, C. M., Villata, M., Carosati, D., et al. 2021, MNRAS, 501, 1100
Raiteri, C. M., Villata, M., Chen, W. P., et al. 2008a, A&A, 485, L17
Raiteri, C. M., Villata, M., Jorstad, S. G., et al. 2023, MNRAS, 522, 102
Raiteri, C. M., Villata, M., Larionov, V. M., et al. 2007, A&A, 473, 819
Raiteri, C. M., Villata, M., Larionov, V. M., et al. 2008b, A&A, 491, 755
Safna, P. Z., Stalin, C. S., Rakshit, S., & Mathew, B. 2020, MNRAS, 498, 3578
Sahakyan, N. 2021, MNRAS, 504, 5074
Sarkar, A., Chitnis, V. R., Gupta, A. C., et al. 2019, ApJ, 887, 185
Sasada, M., Uemura, M., Arai, A., et al. 2010, PASJ, 62, 645
Sasada, M., Uemura, M., Fukazawa, Y., et al. 2014, ApJ, 784, 141
Shields, G. A. 1978, Natur, 272, 706
Singal, A. K. 2016, ApJ, 827, 66
Smith, P. S., Montiel, E., Rightley, S., et al. 2009, arXiv:0912.3621
Spada, M., Ghisellini, G., Lazzati, D., & Celotti, A. 2001, MNRAS, 325, 1559
Stalin, C. S., Gopal-Krishna, Sagar, R., et al. 2006, MNRAS, 366, 1337
Stetson, P. B. 1987, PASP, 99, 191
Stetson, P. B. 1992, JRASC, 86, 71
Stocke, J. T., Morris, S. L., Gioia, I. M., et al. 1991, ApJS, 76, 813
Ulrich, M.-H., Maraschi, L., & Urry, C. M. 1997, ARA&A, 35, 445
Urry, C. M., & Padovani, P. 1995, PASP, 107, 803
Vercellone, S., Striani, E., Vittorini, V., et al. 2011, ApJL, 736, L38
Villata, M., & Raiteri, C. M. 1999, A&A, 347, 30
Villata, M., Raiteri, C. M., Aller, M. F., et al. 2007, A&A, 464, L5
Villata, M., Raiteri, C. M., Balonek, T. J., et al. 2006, A&A, 453, 817
Villata, M., Raiteri, C. M., Gurwell, M. A., et al. 2009, A&A, 504, L9
Villata, M., Raiteri, C. M., Kurtanidze, O. M., et al. 2002, A&A, 390, 407
Villata, M., Raiteri, C. M., Kurtanidze, O. M., et al. 2004, A&A, 421, 103
Villicaña-Pedraza, I., Carreto-Parra, F., Carramiñana, A., & Saucedo-Morales, J. 2017, Galax, 5, 3
von Montigny, C., Bertsch, D. L., Chiang, J., et al. 1995, ApJ, 440, 525
Wagner, S. J., & Witzel, A. 1995, ARA&A, 33, 163
Wehrle, A. E., Marscher, A. P., Jorstad, S. G., et al. 2012, ApJ, 758, 72
Wiita, P. J., Mangalam, A. V., & Chakrabarti, S. K. 1992, in AIP Conf. Proc. 254, Testing the AGN Paradigm, ed. S. S. Holt, S. G. Neff, & C. M. Urry (Melville, NY: AIP), 251
Zhang, B.-K., Zhou, X.-S., Zhao, X.-Y., & Dai, B.-Z. 2015, RAA, 15, 1784